Chapter 2

Experimental Techniques

2.1 Introduction

In this chapter, we describe briefly x-ray diffraction and fluorescence microscopy techniques used to study the phase behaviour of lipid–cholesterol mixtures. Section 2.2 describes the theory of x-ray diffraction with two specific examples of crystal and lamellar phases of amphiphilic molecules. We discuss the phase problem in the context of lamellar structures. The experimental setup used to study diffraction from oriented and unoriented samples are also discussed in this section. Data analysis, including intensity corrections relevant to the present experimental geometry, are discussed in section 2.3. The calculation of the electron density map of the modulated phase, to be discussed in chapter 3, is also presented in this section.

Fluorescence microscopy was used to observe morphological changes as well as phase separation in giant unilamellar vesicles (GUVs). Basic principles of fluorescence confocal microscopy and of two-photon microscopy are illustrated in section 2.4. The preparation of GUVs used in the microscopy studies is described in section 2.5.

2.2 X-ray diffraction

2.2.1 Theory of x-ray diffraction

X-rays are electromagnetic radiation of short wavelength ($\sim$ 1-10 Å). They are scattered by the electrons in the irradiated material. Therefore, the intensity of scattered radiation depends

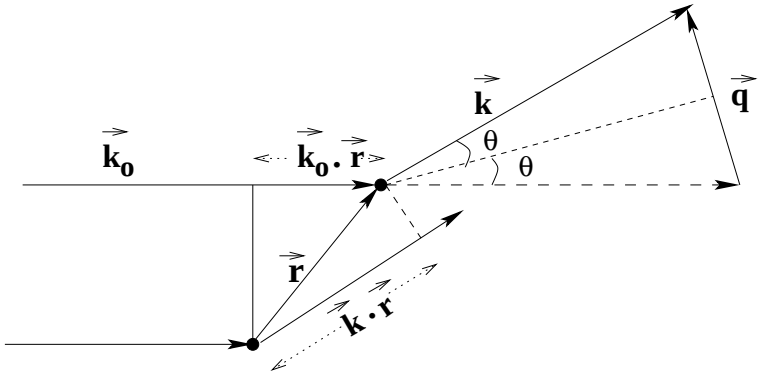

Figure 2.1: Geometric representation of scattering event by two point objects separated by $\vec{r}$.

upon the electron density distribution in the material. The interference of x-rays scattered by different electrons gives rise to the observed diffraction pattern [1, 2, 3].

Let us consider a plane monochromatic wave, $\psi_{in} = \psi_0 e^{i\vec{k_0}.\vec{r}}$, incident on an electron at the origin, where $\vec{k_0}$ is the incident wave vector. Scattering by the electron generates a spherical wave, which at a distance R from the origin can be represented as $\psi_{sc} = \frac{\psi_{in}A}{R} e^{ikR}$, where A is the scattering strength of an electron. Now consider scattering from two electrons, one at origin and the other at a distance r from it. Phase difference between the scattered rays can be written as $(\vec{k} - \vec{k_0}).\vec{r} = \vec{q}.\vec{r}$, where $\vec{q}$ is called the scattering vector. The magnitude of $\vec{q}$ is given by, $|\ \vec{q}\ | = \frac{4\pi sin\theta}{\lambda}$ (Fig. 2.1). The amplitude of the scattered waves can be described as $\psi_{sc} = \frac{\psi_{in}A}{R} e^{i(kR - \vec{q}.\vec{r})}$. If there are N electrons at positions r_i (i=1, 2....N) then the total scattered amplitude at a distance R is

$$\psi_{sc} = \frac{\psi_{in}A}{R} e^{ikR} \sum_{i=1}^{N} e^{-i\vec{q}.\vec{r_i}} \tag{2.1}$$

If we introduce the electron density function $\rho(\vec{r}) = \sum_{i=1}^{N} \delta(\vec{r} - \vec{r_i})$, then the above equation can be written as

$$\psi_{sc} = \frac{\psi_{in}A}{R} e^{ikR} \int \rho(\vec{r}) e^{-i\vec{q}.\vec{r}} d\vec{r} \tag{2.2}$$

Therefore, the amplitude of the scattered wave can be described as the Fourier transform of the electron density function [1]. The scattered intensity is given by

$$I(\vec{q}) = |\ \psi_{sc}\ |^2 = |\ \frac{\psi_{in}A}{R} \int \rho(\vec{r}) e^{-i\vec{q}.\vec{r}} d\vec{r}\ |^2 \ . \tag{2.3}$$

2.2.2 Diffraction by a periodic object

Electron density $\rho(\vec{r})$ of a periodic object can be described as the convolution of a lattice function, $\rho_{lattice}$, which describes the periodicity, with a basis function, ρ_{basis}, which describes the motif present at each lattice point, i.e, $\rho = \rho_{lattice} \otimes \rho_{basis}$. It follows from the convolution theorem that the scattered amplitude, $F(\vec{q})$ is proportional to the product of the Fourier transforms $F_{lattice}$ and F_{basis} of $\rho_{lattice}$ and ρ_{basis}, respectively. Therefore, scattered intensity $I(\vec{q}) = S(\vec{q}).P(\vec{q})$, where the structure factor $S(\vec{q}) = \mid F_{lattice} \mid^2$ determines the points in the reciprocal space where the intensities are sampled, and the form factor $P(\vec{q}) = \mid F_{basis} \mid^2$ determines the intensity at each of these positions. Two specific examples are described below.

2.2.2.1 Crystals

In the case of an infinite crystal, the lattice can be written as

$$\rho_{lattice}(\vec{r}) = \sum_{n_1} \sum_{n_2} \sum_{n_3} \delta(\vec{r} - n_1\vec{a} - n_2\vec{b} - n_3\vec{c}) \tag{2.4}$$

where $\vec{a}$, $\vec{b}$ and $\vec{c}$ are the three primitive translation vectors, and n_1, n_2 and n_3 are integers running from -∞ to +∞. The basis function describing the group of N atoms in the repeating unit is given by

$$\rho_{basis}(\vec{r}) = \sum_{j=1}^{N} \rho_j(\vec{r} - \vec{r_j}) \tag{2.5}$$

where $\rho_j(\vec{r} - \vec{r_j})$ describes the electron density of each atom. The Fourier transform of $\rho_{lattice}(\vec{r})$ is given by

$$F_{lattice}(\vec{q}) = \sum_{h} \sum_{k} \sum_{l} \delta(\vec{q} - h\vec{a^*} - k\vec{b^*} - l\vec{c^*}) \tag{2.6}$$

where $\vec{a^*}$, $\vec{b^*}$ and $\vec{c^*}$ constitute a set of basis vectors in the reciprocal space, and h, k and l are integers running from -∞ to +∞. On Fourier transforming equation 2.5, we get

$$F_{basis}(\vec{q}) = \sum_{j=1}^{N} f_j e^{-i\vec{q}.\vec{r_j}} \tag{2.7}$$

where f_j is called atomic form factor, given by

$$f_j = \int \rho_j(\vec{r}) e^{-i\vec{q}.\vec{r}} d\vec{r}. \tag{2.8}$$

The scattered intensity can be written as

$$I(\vec{q}) \propto | \int \rho(\vec{r}) e^{-i\vec{q}.\vec{r}} d\vec{r} |^2 = \frac{1}{(\vec{a} \times \vec{b}.\vec{c})^2} | F_{basis}(\vec{q}) |^2 \sum_{h,k,l} \delta(\vec{q} - h\vec{a^*} - k\vec{b^*} - l\vec{c^*}). \tag{2.9}$$

Therefore, the diffraction pattern of a crystal consists of a set of peaks, whose positions are determined by the set of Miller indices (*h*, *k* and *l*), whereas intensities are determined by the values of $| F_{basis} |^2$ at these reciprocal lattice peaks. $\vec{a} \times \vec{b}.\vec{c}$ is the volume of a unit cell. Since the intensity is non-zero only at the reciprocal lattice points, it can be written as $I^{hkl} = | F^{hkl} |^2$, where

$$F^{hkl} = \sum_{j=1}^{N} f_j e^{-i(hx_j + ky_j + lz_j)} \tag{2.10}$$

and $\vec{q} = h\vec{a^*} + k\vec{b^*} + l\vec{c^*}$; $\vec{r_j} = x_j\vec{a} + y_j\vec{b} + z_j\vec{c}$.

It is important to mention that F^{hkl} is called the structure factor in crystallography. However, in the small angle scattering literature, intensity is often separated out into a structure factor $S(\vec{q})$ and form factor $P(\vec{q})$, as discussed above.

2.2.2.2 Lamellar phases of amphiphilic molecules

As discussed in the previous chapter, the lamellar phases exhibited by lipid-water systems have a one dimensional (1D) periodicity along the bilayer normal. The lamellar periodicity (*d*) is the sum of the bilayer thickness and the water layer thickness. In the case of a lamellar phase, consisting of N bilayers, the lattice function can be defined as

$$\rho_{lattice}(z) = \sum_{n=0}^{N-1} \delta(z - nd) \tag{2.11}$$

The electron density in the methylene region of the bilayer is very close to that of water and the two can be assumed to be equal to a good approximation. In comparison, the head group region has a higher electron density and the central methyl region has a lower density. The simplest basis function describing the bilayer can be taken to be

$$\rho_{basis}(x, z) = \delta(x)[\rho_H\{\delta(z + x_h) + \delta(z - x_h)\} - \rho_M\delta(z)] \tag{2.12}$$

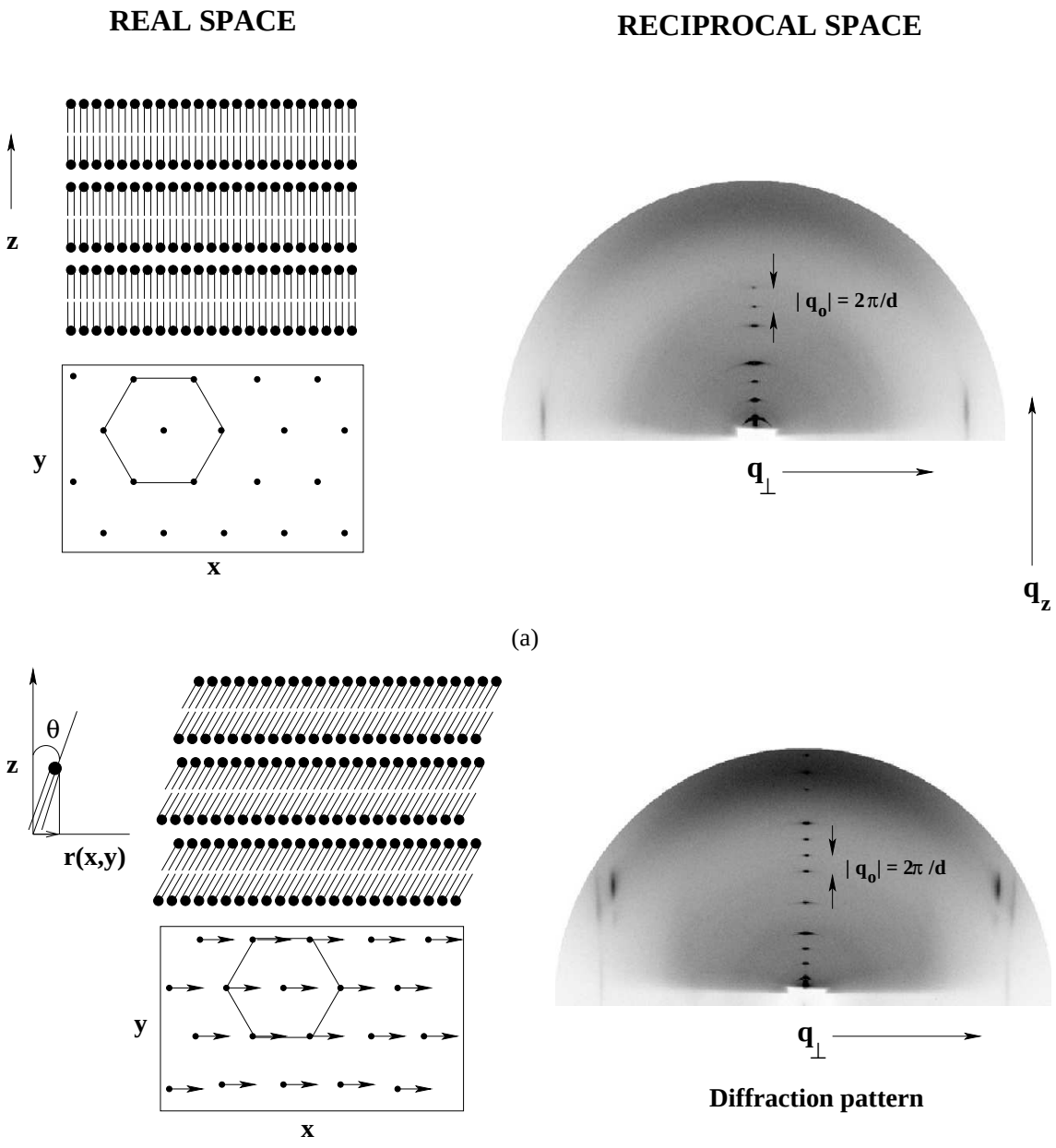

Figure 2.2: Structure of the lamellar gel phases and their corresponding diffraction patterns. Hexagonal lattice of points shown in the box correspond to the arrangement of the hydrocarbon chains in the plane of the bilayers. In the L_β phase shown in (a) the molecules are parallel to the bilayer normal (no tilt). For comparison the diffraction pattern of the $L_{\beta'}$ phase with tilt is shown in (b). The projection of the tilt vector (towards nearest neighbour) on the plane of bilayer is indicated by the arrows at each lattice points. The tilt directions with respect to the laboratory frame of adjacent bilayers are not correlated.

where ρ_H and ρ_M are the electron densities of the head group and terminal methyl group regions, respectively. x_h is the position of the head group from the center of the bilayer. On Fourier transforming the above expressions, we get

$$F_{lattice}(q_z) = \int \sum_{n=0}^{N-1} \delta(z - nd) e^{-iq_z z} dz = \sum_{n=0}^{N-1} e^{-iq_z nd} = e^{-\frac{iq_z d}{2}(N-1)} \frac{sin(\frac{q_z Nd}{2})}{sin(\frac{q_z d}{2})} \tag{2.13}$$

and

$$F_{basis}(q_z) = 2\rho_H cos(q_z x_h) - \rho_M \tag{2.14}$$

Total scattered amplitude is given by

$$F(q_z) = F_{lattice}(q_z).F_{basis}(q_z) \tag{2.15}$$

Maxima of $F_{lattice}(q_z)$ occur when $\frac{q_z d}{2} = n\pi$. Putting $q_z = \frac{4\pi}{\lambda} sin\theta$ in the above condition, we recover the Bragg's law, $2dsin\theta = n\lambda$. Therefore, the diffraction pattern consists of a set of equidistant spots along q_z as shown in Fig. 2.2 [4].

In the fluid phase of the bilayers, the hydrocarbon chains are in a molten state and give rise to a very diffuse peak in the wide angle region of the diffraction pattern. However, as discussed in the previous chapter, in the gel phase the hydrocarbon chains form a two dimensional hexagonal lattice in the plane of the bilayer. Therefore, in-plane structure in the gel phase bilayer can be described as the convolution of a 2D hexagonal lattice and a basis function representing a hydrocarbon chain, which can be taken to be a finite rod with uniform electron density. Fourier transform of the 2D hexagonal lattice of points is a 2D hexagonal lattice of infinite rods, which is rotated by 30° with respect to the real space lattice. The Fourier transform of the basis function is a disc shaped function in the reciprocal space. The product of these two functions gives the structure in the reciprocal space. Consider a gel phase where there is no tilt of the hydrocarbon chains with respect to the bilayer normal. In this case the disc will cut the 6 rods of the hexagonal lattice in the reciprocal space at $q_z = 0$. In our sample geometry the lattice is not aligned in the plane of bilayer. We assume that there are many domains with different in-plane orientations in the irradiated volume of the sample. Therefore, the 6 spots give rise to a single ring. The intersection of this ring with the

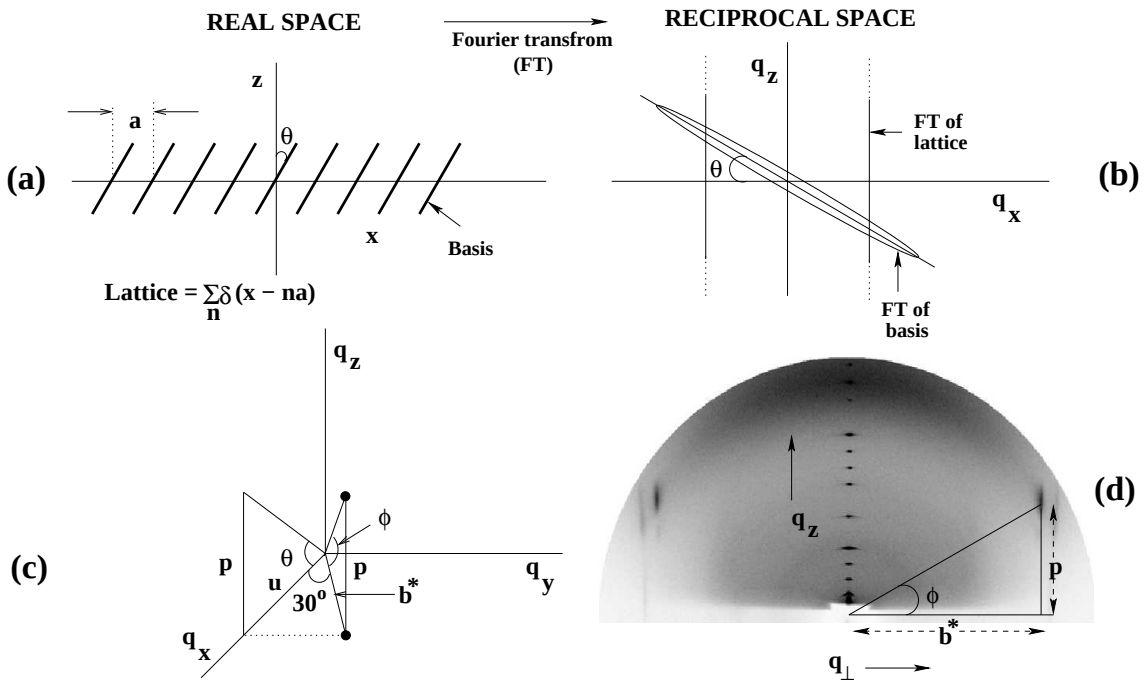

Figure 2.3: A 1D array of tilted rods with tilt angle θ (a) gives rise to a 1D array of infinitely long rods and a finite disc in the reciprocal space (b) corresponding to the Fourier transforms of the lattice and basis, respectively. The disc cuts these rods at an angle corresponding to the tilt angle resulting in two spots in the $q_x - q_z$ plane. As both sign of θ are allowed, there will be two sets of domains, and we get 4 spots in the complete diffraction pattern. A similar analysis can be applied in case of a 2D hexagonal lattice of tilted rods in order to find the tilt angle from the diffraction pattern of the lamellar gel phase. In (c), b^* is the reciprocal lattice vector of the hexagonal lattice. The disc-like function, representing the FT of the chain electron density, is rotated by the tilt angle θ about q_y. ϕ is the angle measured on the diffraction pattern as shown in (d).

Ewald sphere results in two spots on the $q_x - q_y$ (equatorial) plane as shown in Fig. 2.2 a. For tilted hydrocarbon chains, the disc will cut the 6 rods at an angle θ corresponding to the tilt angle with respect to bilayer normal (This has been illustrated for the case of a 1D array of rods in Fig. 2.3 a and b). Therefore, we get 6 spots, three above the equatorial plane ($q_z = 0$) and three below it. As the lattice is unoriented in the plane, rotation of these three spots form three rings. The intersection of these rings with the Ewald sphere will give 6 diffraction spots, three on either side of the equatorial plane. These three reflections will be at $q_z \neq 0$ for an arbitrary tilt direction (Fig. 2.4 a) [5]. If the tilt direction is towards nearest neighbour, then two spots will merge at the equatorial plane giving rise to one spot at $q_z = 0$ and the other at $q_z \neq 0$ as shown in Fig. 2.4 b [6]. The tilt axis is along q_y and makes an angle of 60° with respect to b^* (Fig. 2.3 c). From the simple geometric consideration shown in Fig. 2.3 c and d, we get $tan\phi = \frac{p}{b^*}$ and $tan\theta = \frac{p}{u}$. Now for a hexagonal lattice $\frac{u}{b^*} = sin60°$. Therefore, the tilt angle can be calculated using the following equation

$$tan\theta = \frac{tan\phi}{sin60°} \tag{2.16}$$

In the case of tilt towards next nearest neighbour, two rings merge and give rise to a spot at $q_z \neq 0$ and the third ring results in a spot at a larger q_z (Fig. 2.4 c). In this case the tilt axis makes an angle of 90° with b^* and hence $tan\theta = tan\phi$, where ϕ corresponds to the reflection with larger q_z. It is clear from the above analysis that the diffraction pattern of the gel phase, shown in Fig. 2.2 b, corresponds to molecular tilt towards nearest neighbour. The two additional off-axis weak reflections seen in the diffraction pattern are the secondary maxima of the reflection at $q_z = 0$. They arise from the secondary maxima of the chain form factor.

2.2.3 The phase problem in crystallography

In general, the structure factor $F(\vec{q}) = \int \rho(\vec{r}) e^{-i\vec{q}.\vec{r}} d\vec{r}$ is a complex quantity. Therefore, to calculate the electron density $\rho(\vec{r})$ one needs to know both the amplitude and phase of $F(\vec{q})$. Since $I(\vec{q}) = | F(\vec{q}) |^2$, only the magnitude of $F(\vec{q})$ is known from a diffraction experiment, but the phase information is lost. For a non centro-symmetric system phases can be arbitrary,

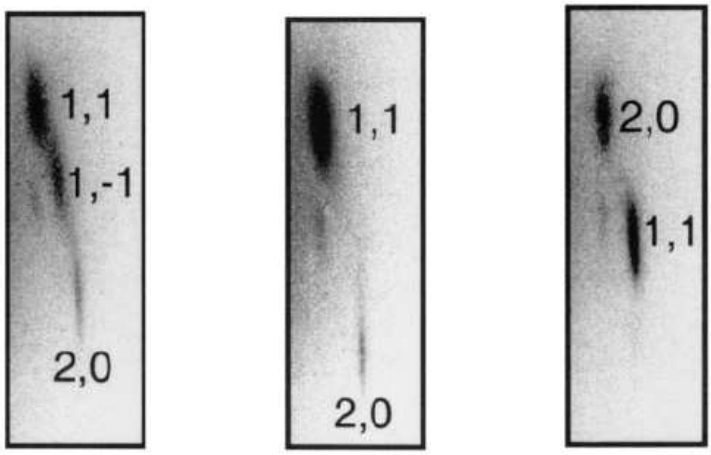

(a) (b) (c)

Figure 2.4: Wide angle chain reflections from three different types of gel phases as discussed in chapter 1. The direction of chain tilt is towards arbitraty direction (a), nearest neighbour (b) and next nearest neighbour (c) [5]. Reflections are indexed on a hexagonal chain lattice, as shown.

but for a centro-symmetric system i.e, when $\rho(-\vec{r}) = \rho(\vec{r})$, phases are constrained to be either 0 or π.

There are several methods to retrieve the phase information from the experimental data. Let us discuss the phase problem in the context of membrane structures. A bilayer possesses center of symmetry and therefore, for n reflections, 2^n combinations of phases are possible. If there are only a few reflections (3 to 4), then the phase of one of the reflections can be fixed and other phases can be determined by calculating the electron density with all possible combinations. Ideally only one and in practice only few of these combinations result in acceptable electron density profiles. For a large number of reflections this method is extremely laborious and hence one needs some alternative methods to obtain the phases. Two such methods are described below.

In the case of lamellar phase the repeat distance d is the only lattice parameter. Therefore, on swelling and shrinking the lamellar phase without altering the membrane structure we can essentially sample $F(\vec{q})$ at different points in the reciprocal space [7]. Since $F(\vec{q})$ is real, its sign can be obtained from the distribution of zeros. Therefore, once the phase of the 1^{st} order reflection is fixed, those of others follow from the zeros of $F(\vec{q})$ (Fig. 2.5).

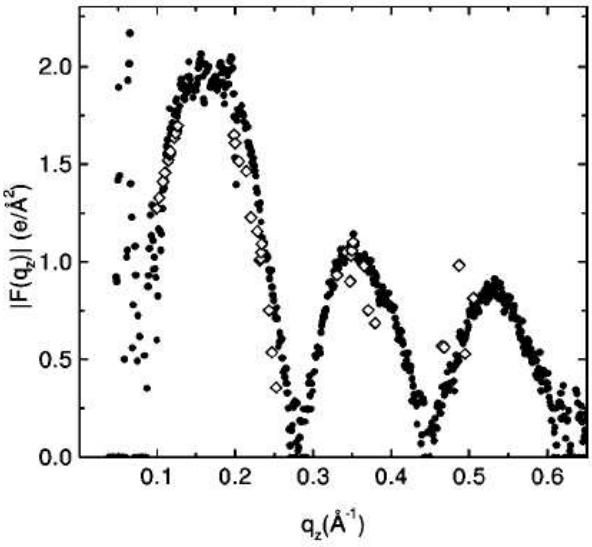

Figure 2.5: Plot of the magnitude of the membrane form factor, | $F(q_z)$ | as a function of q_z obtained from a swelling experiment [7].

Another way to retrieve phases is to have an appropriate model for the electron density with a few adjustable parameters. By fitting the calculated structure factor with experimentally observed data, one can determine the unknown parameters of the model and hence the electron density map [8]. This modeling approach will be described in detail in section 2.3.2.

Direct methods have also been used to determine the phases of reflections from a lamellar phase and to calculate the electron density profile [9].

2.2.4 Experimental setup

For diffraction studies, unoriented samples were taken in glass capillaries (*Hampton Research*) having a diameter of 1 mm. They were placed inside a locally built heater, whose temperature could be controlled using a standard PID (Proportion-Integral-Derivative) controller program to an accuracy of ± 0.1°C. Typical experimental setup for unoriented samples is shown in Fig. 2.6.

For aligned samples, a locally built heater is used which is made up of a double walled nickel-plated brass chamber through which water can be circulated [10]. Temperature of the heater can be changed by circulating water at the desired temperature from a water bath (*Julabo*). The inlet and outlet windows of the chamber were covered with mylar sheets. The

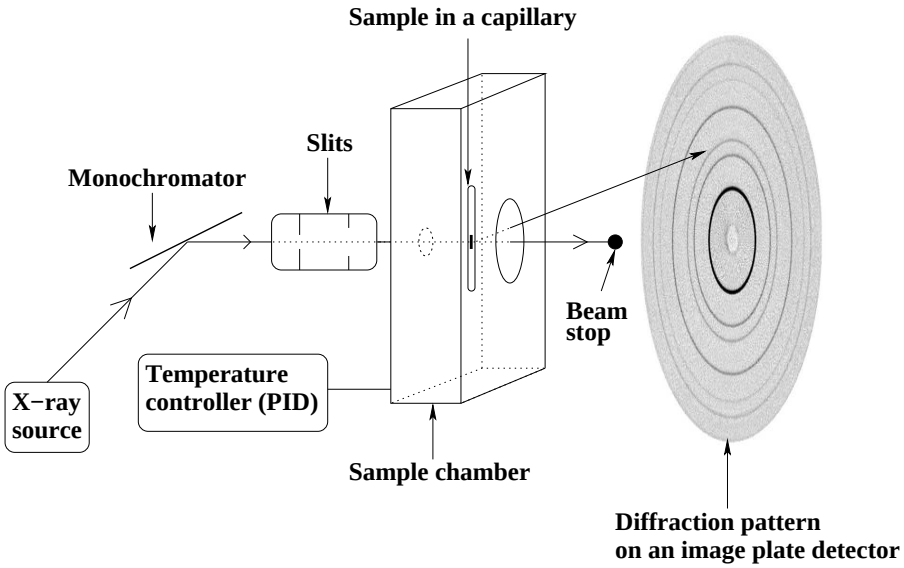

Figure 2.6: Experimental setup for x-ray diffraction of unoriented samples.

chamber was made airtight to achieve a constant relative humidity (RH) inside (Fig. 2.7). High RH close to 100 % was achieved by keeping a reservoir of water inside the chamber. Lower values of RH were obtained using saturated salt solutions. A small electric fan is used to maintain the temperature and RH uniform inside the chamber. Water condensation on the inlet and outlet windows due to high temperature differences between the inside and the outside was prevented by gently blowing hot air on the windows. A thermo-hygrometer probe (*Testo 610*) was inserted into the chamber to monitor both the temperature and RH close to the sample.

2.2.5 Preparation of oriented samples

All lipids, cholesterol and other chemicals used in the experiments were purchased from *Fluka* and *Sigma* and were used without further purification.

Appropriate amounts of the lipid and cholesterol were dissolved in chloroform. Typical total concentration was ~ 5 mg/ml. The sample was deposited on the outer surface of a glass beaker (radius ≈ 17 mm). The beaker was kept overnight inside an evacuated desiccator to remove all traces of the solvent. Typical area density of dried lipid film was $\sim 5\ \mu$g/mm^2. It was then kept inside a sealed airtight container along with some Millipore (ultrapure) water

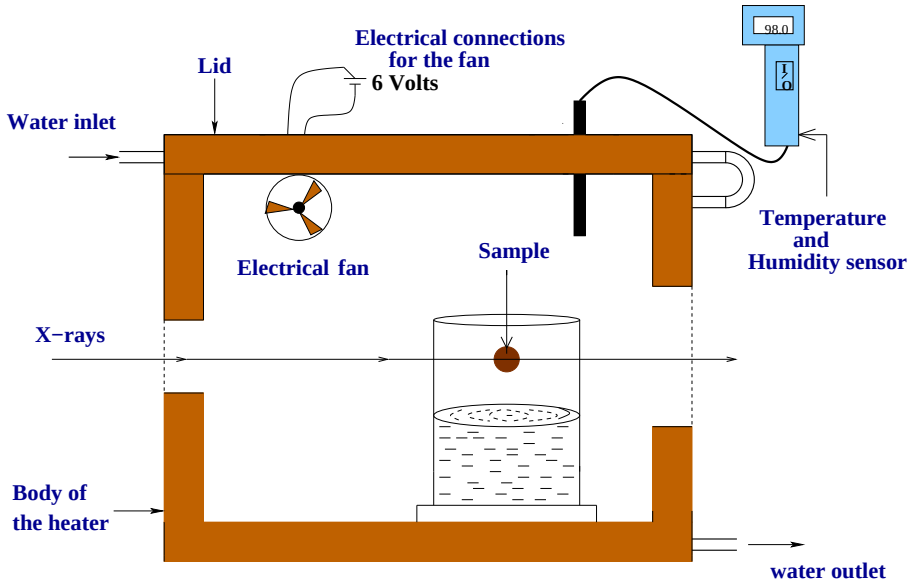

Figure 2.7: Humidity chamber used for x-ray diffraction from aligned samples

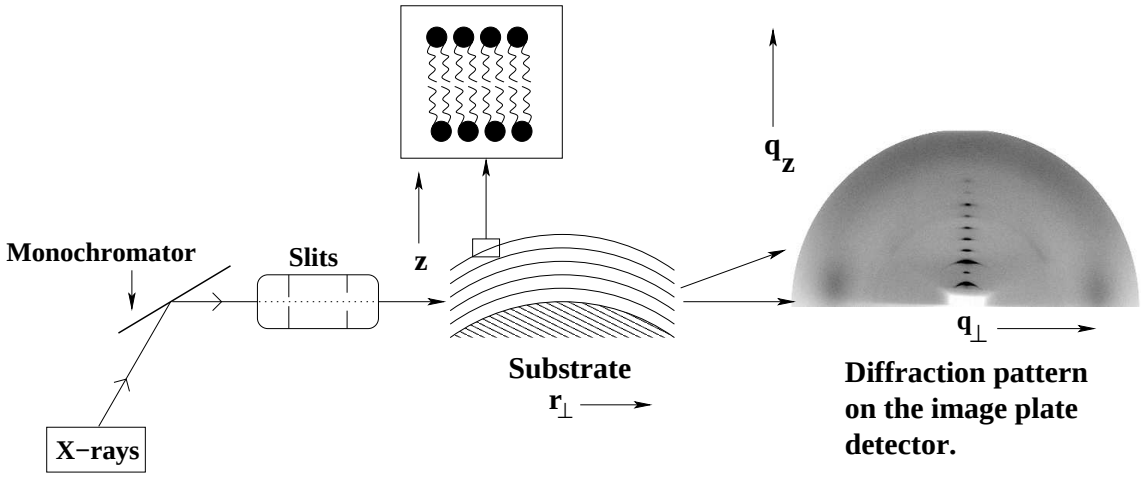

Figure 2.8: Experimental geometry for aligned samples

for a couple of days. Cycling the temperature of the sample across the main transition a few times while hydrating results in a well oriented sample, where the bilayers are oriented parallel to the substrate. The sample was then transfered to the sealed chamber, described in the previous section, for experiments.

2.2.6 Data collection

X-rays were generated from a rotating anode generator (*Rigaku UltraX 18*) operating at 50 KV and 80 mA. CuK_α radiation (λ = 1.54 Å) was selected using a flat graphite monochroma-

tor (*Huber*). Monochromatic x-rays then pass through a collimator which consists of two sets of slits. Adjusting the slits we can obtain required beam size at the sample and avoid parasitic scattering. Typical beam diameter after collimation was ~ 1mm. X-rays were incident tangential to the cylindrical substrate (glass beaker), with the cylinder axis normal to the beam. Typical experimental geometry is shown in Fig. 2.8. Diffraction patterns were recorded on a 2D image plate detector (*Marresearch*) on cooling the sample. We have also recorded some diffraction patterns during the initial heating of the sample. Diffraction patterns recorded on the image plate detector (diameter 180 or 240 mm) were scanned and transfered to a computer in the form of 16 bit binary data using a software provided by Marresearch for data collection. The pixel size was 100 μm. Typical exposure time was ~ 1 hour. Sample to detector distance was determined using a standard sample. Typical sample to detector distance (D) was ~ 200-260 mm.

In the case of oriented sample on a flat substrate, one needs to rotate the sample in order to obtain many diffraction spots. Using a curved substrate is equivalent to rotating the sample by a small angle. This results in an increased effective mosaicity of the sample, which is sufficient to obtained all the reflections from the lamellar phases.

2.3 Data analysis

Diffraction patterns collected on the image plate were viewed and analyzed using the software provided by Marresearch. Diffraction pattern from an unoriented sample consists of concentric rings as shown in Fig. 2.9. The corresponding values of d (= $\frac{n\lambda}{2sin\theta}$) and q (= $\frac{4\pi sin\theta}{\lambda}$) were calculated from the radius (R) of the diffracted ring by evaluating θ (= $\frac{1}{2}tan^{-1}\frac{R}{D}$), where D is the sample to detector distance. The integrated intensity $I(q)$ versus q was obtained by integrating over the azimuthal angle.

The diffraction pattern from an oriented sample consists of isolated spots in the $q_z - q_\perp$ plane as shown in Fig. 2.10. As discussed earlier, diffraction pattern from an oriented lamellar phase consists of equidistant spots along q_z. In case of lamellar phases exhibited by lipid bilayers, these reflections are usually called the main reflections. Reflections in the

Figure 2.9: Diffraction pattern from an unoriented sample in the gel phase. Concentric rings in the small angle region correspond to the lamellar reflections . Sharp ring in the wide angle region is the reflection from the in-plane hexagonal lattice of the hydrocarbon chains. The diffuse ring at intermediate angles is due to the mylar window of the sample chamber.

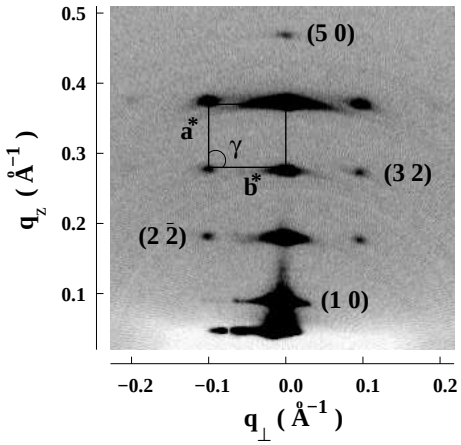

Figure 2.10: Small angle region of the diffraction pattern from an oriented sample. This pattern corresponds to the modulated structure (P_β phase) of the bilayers. The box shows a rectangular unit cell of the reciprocal lattice.

$q_\perp \neq 0$, known as satellite reflections, are seen in phases where the bilayers have periodic modulations. (Fig. 2.10). Lattice parameters (a^*, b^* and γ) can be directly read off from the diffraction pattern in the case of a two dimensional lattice. To obtain integrated intensity, a rectangular box which covers the entire spot was drawn with its edges parallel to $q_\perp$ and q_z . $I(q)$ versus q curves were obtained by integrating along one of the edges of the box after subtracting the background. The background was assumed to be linear across each diffraction peak. Intensity profile was obtained from a fit to a Gaussian after background subtraction. Gaussian fit was especially required to resolve two partially overlapping peaks.

The diffraction pattern corresponding to the modulated structure of bilayers shown in Fig. 2.10 was obtained from a DPPC-cholesterol mixture. This will be discussed in detail in chapter 3. We refer to it as the P_β phase. Below we discuss the intensity corrections relevant to this phase in the present experimental geometry and then the model for calculating the electron density map of this phase. The height modulation of the different bilayers in the P_β phase are correlated and form a rectangular unit cell (Fig. 2.11 a) with lattice parameters $\vec{a} = d\hat{z}$ and $\vec{b} = \lambda_r \hat{x}$. d and λ_r are the bilayer repeat distance and the wavelength of the modulation, respectively. The corresponding lattice parameters in the reciprocal space are given by $\vec{a^*} = \frac{2\pi}{d}\hat{q_z}$ and $\vec{b^*} = \frac{2\pi}{\lambda_r}\hat{q_x}$.

2.3.1 Intensity corrections

2.3.1.1 Geometric corrections

In an ideal situation, diffraction from a 1D modulated structure (ripple), which forms a rectangular unit cell, gives rise to a diffraction pattern shown in Fig. 2.11 a. If the ripple direction is not fixed in the x-y plane then the spots at $q_x \neq 0$ become rings in the q_x - q_y plane around the spots along q_z, as shown in Fig. 2.11 b. Now let us consider a practical situation where the modulated structure is formed by the lipid bilayers. In the present experimental geometry, bilayers are aligned parallel to the curved substrate but the ripple direction is not fixed. In other words, there are domains in the plane of the bilayer with all possible orientations of the ripple. Unlike the ideal situation discussed above, the diffraction spot obtained from an

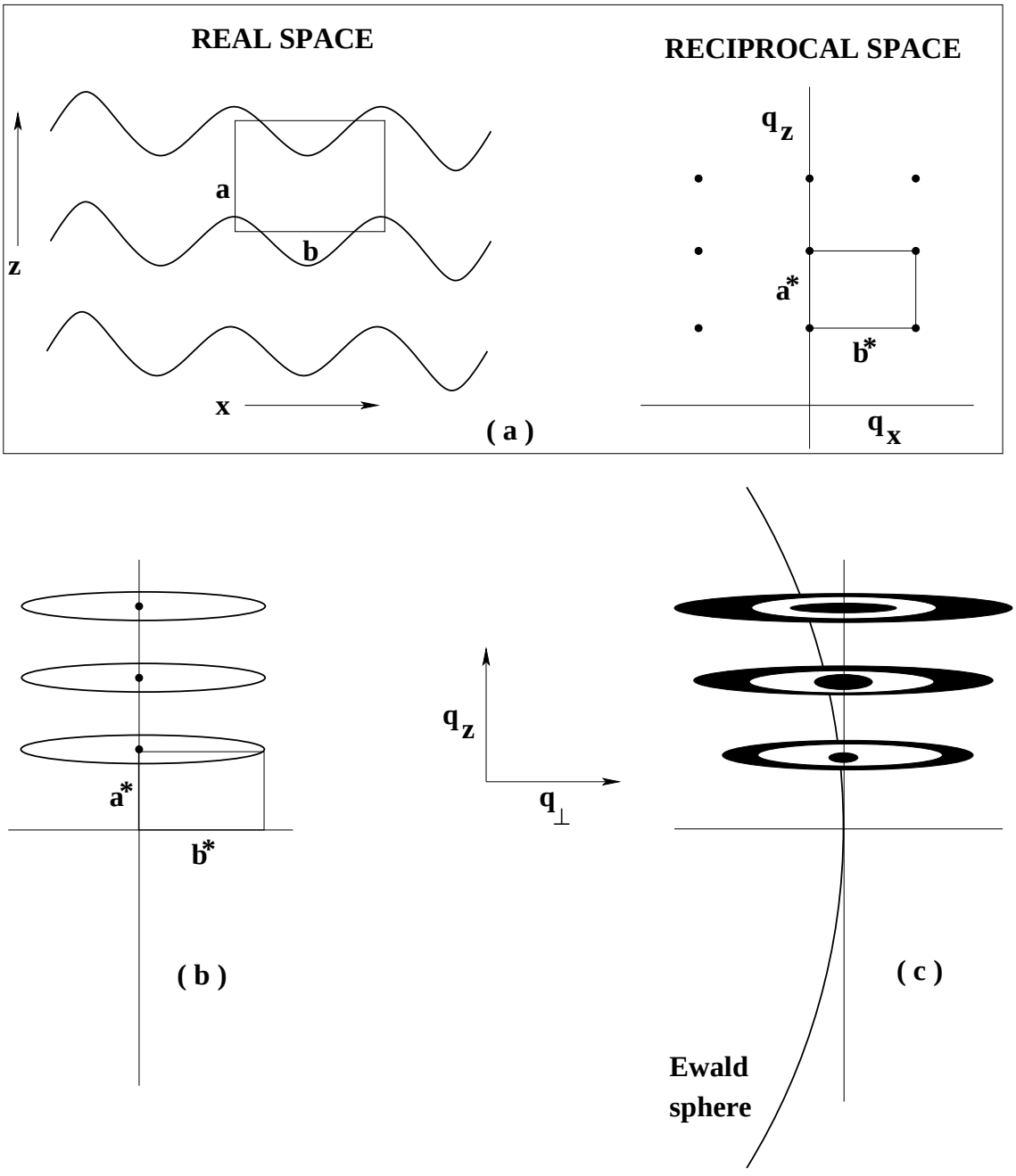

Figure 2.11: The reciprocal lattice structure of a modulated phase. (a) The rectangular unit cell in the reciprocal space corresponding to the modulated structure when the modulation is along x. If the modulation direction is not fixed in the x-y plane then each spot will form a ring in the $q_x - q_y$ plane as shown in (b). In practice, these reflections get broadened and smeared out due to the sample mosaicity (c) as described in the text.

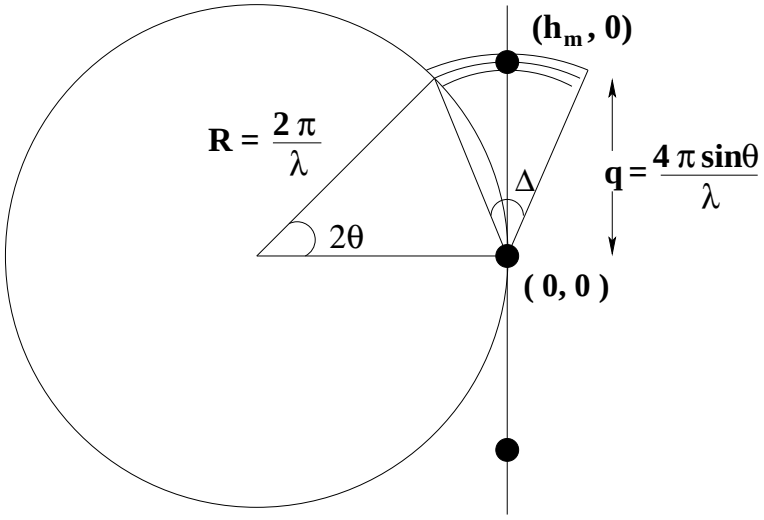

Figure 2.12: Calculation of geometric correction for the main reflections. The circle represents the Ewald sphere. (h_m, 0) is the highest order reflection observed in the diffraction pattern. q is the distance of m^{th} order reflection from the origin of the reciprocal space. $q\Delta$ is the linear spread of the m^{th} order reflection, where Δ is the sample mosaicity. From the geometry, we get $\Delta = 2\theta_m$, where the θ_m is the Bragg's angle corresponding to the m^{th} order reflection. The estimated Δ is found to be $\sim 10^{\circ}$.

aligned sample is not a geometrical point, but is smeared out due to the finite extension of the sample, the finite angular spread of the incident x-rays, and the mosaicity of the sample. In practice, the lamellar reflections become arcs with an angle Δ subtended at the origin of the reciprocal space and the satellite reflections form distorted rings as depicted in Fig. 2.11 c. The cross section of the ring gets broadened due to the above mentioned reasons. The observed reflections can be thought of as the intersection of these arcs and the rings with the Ewald sphere. Therefore, the geometric correction for the lamellar reflections (main reflections) is different from that for the satellite reflections. Intensity corrections are required in order to put all the reflections on the same intensity scale.

As Δ is same for all the reflections, the length of the arc is larger for higher order main reflections and hence the reduction in the intensity will be more at larger angles (Fig. 2.12) [11]. Therefore, observed intensity (I_o) needs to be multiplied by the length of the arc, given by $q\Delta$. Due to the finite width of the arc, an additional factor of $cos\theta$ has to be included as the Ewald sphere cuts the arc at an angle θ (Fig. 2.12). Therefore, the corrected intensity (I_c)

for the main reflections can be written as

$$I_c = I_o q \Delta cos\theta = I_o \frac{2\pi\Delta}{\lambda} sin2\theta \tag{2.17}$$

Estimated value of Δ (mosaicity) is about 10°, as illustrated in Fig. 2.12. [11].

As shown in Fig. 2.11 c, satellite reflections form rings around the lamellar reflections and the intersection of these rings with the Ewald sphere gives rise to two equivalent spots in the observed diffraction pattern. Since the Ewald sphere cuts the ring at a small angle the angular dependence of these spots is weak. Therefore, the observed intensity (I_o) has to be multiplied by the perimeter of the ring to obtain the corrected intensity (I_c). The radius of the ring (R') is given by $\frac{2\pi|k|}{\lambda_r}$, where k is the Miller index of the corresponding reflection.

$$I_c = I_o 2\pi R' = I_o \frac{4\pi^2}{\lambda_r} \mid k \mid \tag{2.18}$$

2.3.1.2 Absorption corrections

Since samples were aligned on a curved substrate, x-rays traverse different paths in different parts of the sample. Therefore, the reduction of both the incident and scattered intensity due to the absorption of x-rays by the sample are different for different reflections. However, we have not applied absorption corrections as it is difficult to measure the thickness of the sample accurately. Previous study on the $P_{\beta'}$ phase has shown that the electron density map is not affected much by neglecting absorption corrections [11].

2.3.2 Modeling of the electron density of the modulated (P_β) phase

It is clear from the diffraction patterns that the P_β phase has a simple rectangular unit cell (Fig. 2.10). The bilayers in this phase, therefore, must have a periodic modulation (Fig. 2.13). We take this to be a height modulation, as in the ripple ($P_{\beta'}$) phase. We rule out a thickness modulation of the bilayers, since packing considerations in such a case can be expected to favour a centered rectangular unit cell. The electron density can be calculated from the diffraction data, once the phases of the different reflections are known. Since the bilayer has a center of symmetry, the phases are either 0 or π, and can be determined using

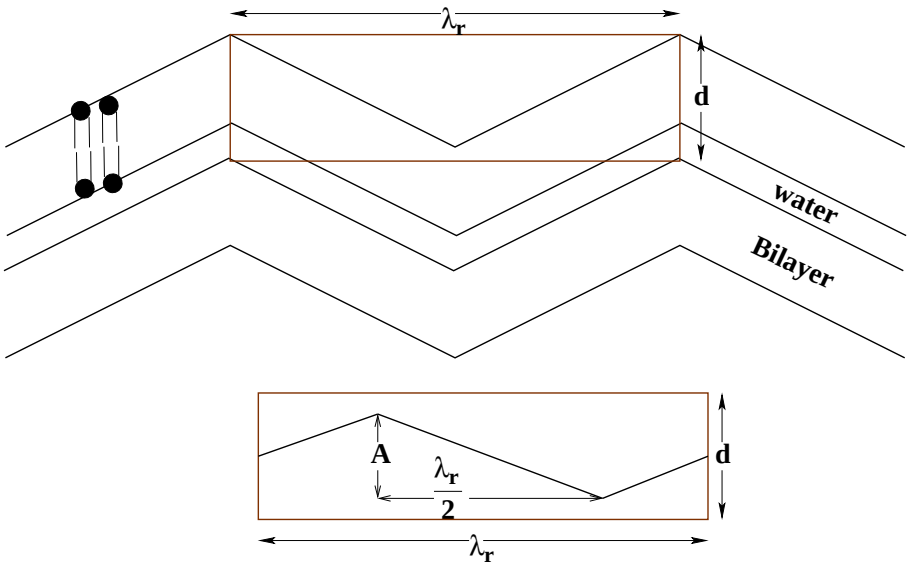

Figure 2.13: The model used for calculating the electron density map (EDM) of the P_β phase. d: bilayer periodicity ; A and λ_r are the amplitude and the wavelength of the modulation, respectively.

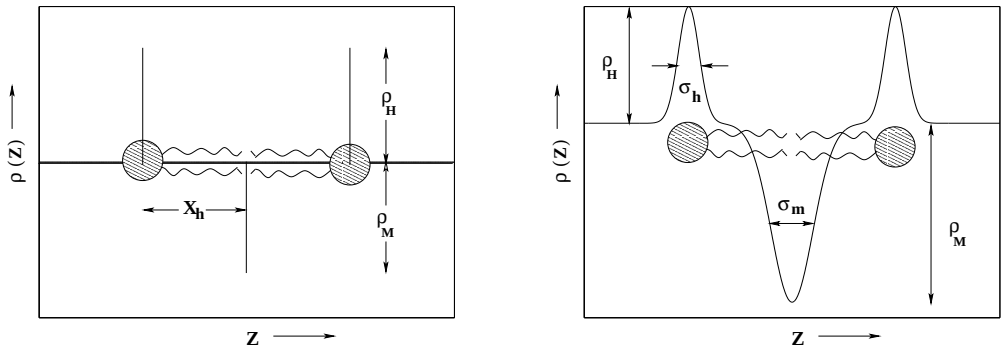

Figure 2.14: (a) Three delta function and (b) Gaussian models for trans-bilayer electron density profile. ρ_H and ρ_M are the heights of the delta functions and Gaussian profiles corresponding to the electron density of head groups and terminal methyl groups, respectively. x_h is the distance of head group from the center of the bilayer. σ_h and σ_m are the widths of the Gaussians corresponding to the head group and terminal methyl group, respectively.

a modeling procedure used earlier for the $P_{\beta'}$ phase [8, 11]. The electron density within the unit cell $\rho(r)$ can be described as the convolution of a contour function $C(x,z)$ and a transbilayer profile $T(x,z)$, i.e., $\rho(r) = C(x,z) \otimes T(x,z)$. $C(x,z) = \delta[z - u(x)]$, where $u(x)$ describes the bilayer height profile (Fig. 2.13). The calculated structure factors F_c are the Fourier transform $F(\vec{q})$ of $\rho(r)$ sampled at the reciprocal lattice points. From the convolution theorem it follows that $F(\vec{q})$ is given by

$$F(\vec{q}) = F_C(\vec{q}).F_T(\vec{q}) \tag{2.19}$$

where $F_C(\vec{q})$ and $F_T(\vec{q})$ are the Fourier transforms of $C(x,z)$ and $T(x,z)$, respectively. $u(x)$ is assumed to have a triangular shape, given by

$$\begin{aligned} u(x) &= \frac{2A}{\lambda_r}(x + \frac{\lambda_r}{2}) && -\frac{\lambda_r}{2} \leq x < -\frac{\lambda_r}{4} \\ &= -\frac{2A}{\lambda_r}x && -\frac{\lambda_r}{4} \leq x \leq \frac{\lambda_r}{4} \\ &= \frac{2A}{\lambda_r}(x - \frac{\lambda_r}{2}) && \frac{\lambda_r}{4} < x \leq \frac{\lambda_r}{2} \end{aligned}$$

where A and λ_r are the amplitude and the wavelength of the modulation, respectively. On Fourier transforming $C(x,z)$, we get

$$\begin{aligned} F_C(\vec{q}) &= \frac{1}{\lambda_r}\int_{-\frac{\lambda_r}{2}}^{\frac{\lambda_r}{2}} C(x,z)e^{-i(q_x x + q_z z)}dxdz \\ &= \frac{1}{2}\frac{sin\omega}{\omega} + \frac{1}{2}\frac{cos\frac{1}{2}(\frac{q_x\lambda_r}{2} + \omega)}{cos\frac{1}{2}(\frac{q_x\lambda_r}{2} - \omega)}\frac{sin(\frac{q_x\lambda_r}{2} - \omega)}{(\frac{q_x\lambda_r}{2} - \omega)} \end{aligned}$$

where $\omega = \frac{1}{4}(q_x\lambda_r + 2q_zA)$.

2.3.2.1 Transbilayer electron density profile ($T(x,z)$)

We have considered different models for the transbilayer electron density profile discussed below.

Simple delta function model (SDF):

$T(x,z)$ consists of three delta functions, two with positive amplitude (ρ_H) corresponding to

the head group regions at the surfaces of the bilayer, and one with negative amplitude (ρ_M) corresponding to the methyl group regions at the center of the bilayer (Fig. 2.14 a). It is given by

$$T(x,z) = \delta(x)[\rho_H\{\delta(z + x_h) + \delta(z - x_h)\} - \rho_M\delta(z)] \tag{2.20}$$

where x_h is the position of the head group with respect to the center of the bilayer. Fourier transforming the above equation, we get

$$F_T(\vec{q}) = \rho_M[\frac{2\rho_H}{\rho_M}cos(x_h q_z) - 1] \tag{2.21}$$

If the bilayers contain cholesterol, the electron density exhibits two more local maxima [12]. Therefore, the electron density of cholesterol containing bilayers can be modeled with five delta functions. In this case $F_T(\vec{q})$ can be written as

$$F_T(\vec{q}) = \rho_M[\frac{2\rho_H}{\rho_M}cos(x_h q_z) + \frac{2\rho_C}{\rho_M}cos(x_c q_z) - 1] \tag{2.22}$$

where ρ_C and x_c are the amplitude and the position of delta function, respectively, from the center of the bilayer corresponding to the cholesterol molecule.

Gaussian model:

The SDF is an oversimplified model to represent head groups and chains. In the Gaussian model, the three delta functions described above are replaced by three Gaussians of widths σ_h and σ_m corresponding to the head group and terminal methyl group regions, respectively (Fig. 2.14 b). The transbilayer electron density using the Gaussian model can be described as

$$T(x,z) = \delta(x)[\rho_H\{e^{-\frac{(z+x_h)^2}{2\sigma_h^2}} + e^{-\frac{(z-x_h)^2}{2\sigma_h^2}}\} - \rho_M e^{-\frac{z^2}{2\sigma_m^2}}] \tag{2.23}$$

Fourier transforming the above equation, we get

$$F_T(\vec{q}) = \sigma_m\rho_M[\frac{2\rho_H\sigma_h}{\rho_M\sigma_m}\{e^{-\frac{q^2\sigma_h^2}{2}}cos(q_z x_h)\} - e^{-\frac{q^2\sigma_m^2}{2}}] \tag{2.24}$$

The observed structure factor magnitudes ($|F_o^{hk}|$) were obtained from the integrated intensity calculated from the diffraction data ($|F_o^{hk}| = \sqrt{I^{hk}}$). Geometric corrections to the observed intensities, relevant to the present experimental geometry, are discussed in the

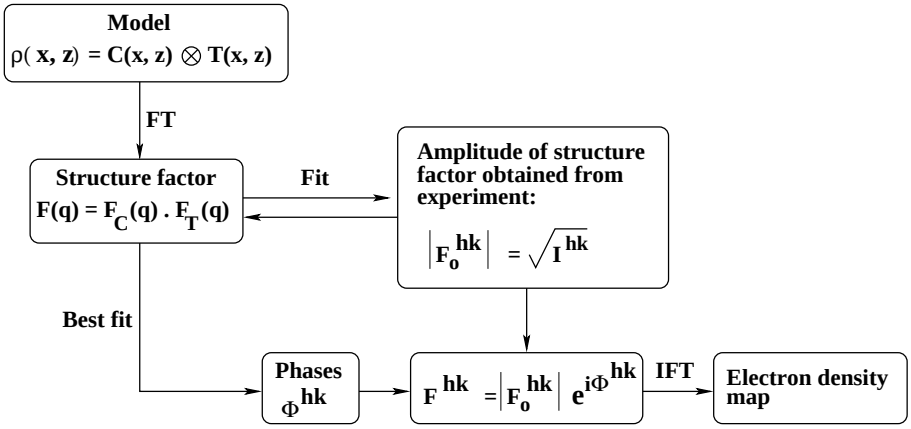

Figure 2.15: Schematic flow diagram of the fitting procedure. FT and IFT represent the Fourier transforms and inverse Fourier transforms.

previous section. Let the calculated structure factor evaluated at each q, corresponding to each observed diffraction spot be F_c^{kh}. Then we define a quantity, given by:

$$\Sigma = \sum_{h,k} \| F_c^{hk} | - | F_o^{hk} \|^2 \tag{2.25}$$

The best fit of the calculated structure factors with the observed ones can be obtained by minimizing Σ. This was done by using the standard Levenberg Marquardt technique for nonlinear least squares fitting [13]. Flow diagram for calculating electron density map is shown in Fig. 2.15. Parameters in these models, such as ρ_H, ρ_M, ρ_C and the bilayer thickness, are determined from the best fit. The calculated structure factors, F_c^{hk} using best fit model parameters carry the phase (Φ^{hk}) information, i.e, $e^{i\Phi^{hk}} = \frac{F_c^{hk}}{|F_c^{hk}|} = \pm 1$. The calculated phases (Φ^{hk}) obtained from the model with best fit parameters were combined with the observed magnitudes, and inverse Fourier transformed to get the two-dimensional electron density map, using the expression,

$$\rho(x,z) = \sum_{h,k} F_o^{hk} e^{i\Phi^{hk}} cos(q_x^{hk} x + q_z^{hk} z) \tag{2.26}$$

2.4 Light microscopy

We have studied giant unilamellar vesicles (GUVs) which are single bilayer shells having a diameter in the range 10 - 100 μm (Fig. 2.16), using optical microscopy. The results of these

studies are described in chapter 7. Here we discuss the basic principles of confocal fluorescence microscopy and the preparation of GUVs. GUVs are transparent to light and hence cannot be visualized using conventional bright field light microscopy. Therefore, one needs to use phase contrast or differential interference contrast (DIC) to observe GUVs [14]. Fluorescence microscopy can also be used to visualize them [15]. Changes in the morphology of GUVs can be directly observed using phase contrast or DIC. However, phase separation in the bilayers in GUVs made up of a lipid mixture can only be visualized using fluorescence microscopy. Preferential partitioning of a fluorescence dye into one of the coexisting phases creates a contrast between the two phases and hence phase separation can be detected in the microscope.

2.4.1 Fluorescence microscopy

When electrons from a fluorescent material are excited from the ground state to a higher electronic energy level, they undergo a non radiative decay and relax to a lower vibrational level of the same excited state. The electrons then return to the ground state via emitting photons of a higher wavelength relative to the incident photons. This process is termed as fluorescence. The fluorescent material are also known as fluorophores. Typical fluorescence life time (the average time spent in the excited state before it returns to the ground state) is $\sim$ 10 ns [15].

In fluorescence microscopy, a specimen which is labeled with fluorophores is excited by radiation of an appropriate wavelength and the emission is detected using a charge couple device (CCD) or photomultiplier tube (PMT).

2.4.1.1 Principles of confocal fluorescence microscopy

Confocal microscopy is a widely used experimental tool for imaging thick samples (like biological cells, tissues etc) at high resolution which is not possible to achieve in conventional bright field light microscopy. In conventional bright field light microscopy, the image of a thick specimen (5 to 10 μm thickness) will be blurred due to the presence of light emerging

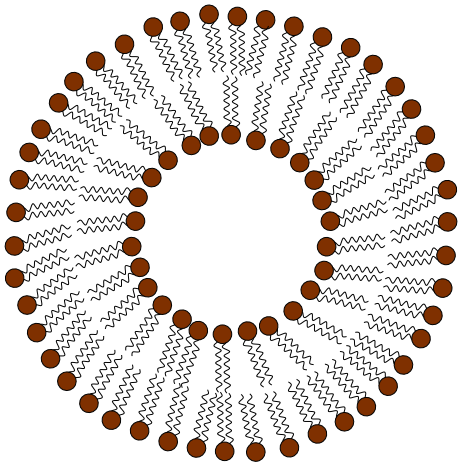

Figure 2.16: Schematic diagram of a unilamellar vesicle

from outside the focal plane of the objective lens and thereby the image resolution is poor. In other words, information from different planes of the specimen cannot be resolved with high resolution in conventional light microscopy. This problem is solved with confocal microscopy and light from outside the focal plane of the objective (objective plane) is blocked using a confocal aperture (pinhole) placed in the plane conjugate to the focal plane of the objective in front of the detector.

In a laser scanning confocal fluorescence microscopy, a laser of an appropriate wavelength is used to excite the fluorophore attached to the sample. Laser is focused onto the specimen at a point in the focal plane of the objective. The point of focus acts as a point source and the diffracted light at the back focal plane of the objective forms concentric Airy discs. Therefore, the image of a point source will not be a point but is spread out (point spread function). Confocality is achieved by allowing light only from the first Airy disc using a pinhole aperture before the detector. This is equivalent to the collection of emitted light only from the focal plane. The optimum pinhole size is dependent on the objective magnification and the numerical aperture (NA) of the objective. Typical optical path of a laser scanning microscope is shown in Fig. 2.17. In brief, light of an appropriate wavelength is reflected by the dichroic mirror and gets focused onto the specimen by the objective. The emitted light passes through the dichroic mirror and is detected using a PMT via a pinhole. Light emerging from outside the focal plane is not detected by the PMT as shown by the

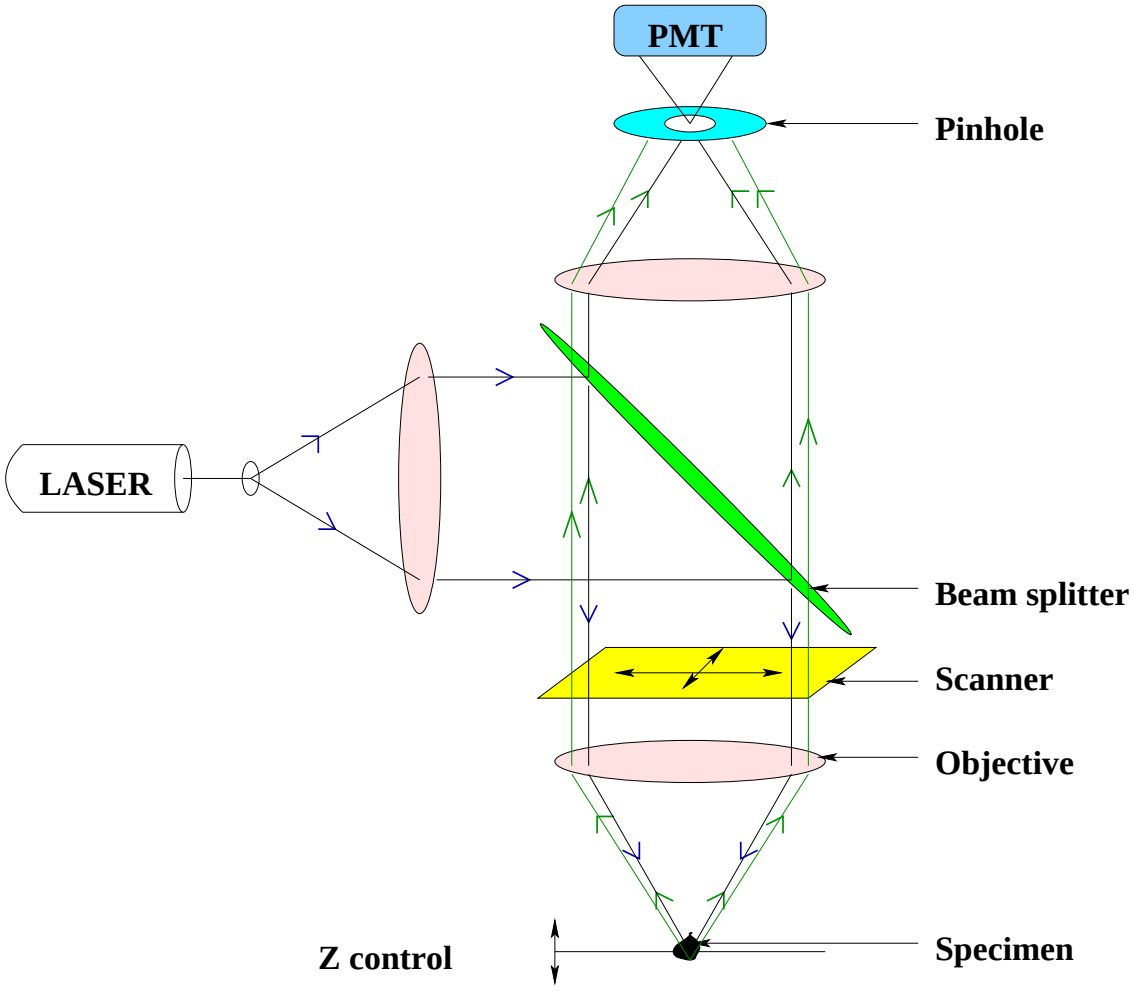

Figure 2.17: Light path in the laser scanning confocal fluorescence microscope.

green rays. In order to obtain entire image of the specimen plane, the specimen is scanned by deflecting the laser focus along the X-Y plane. Once the entire plane of the specimen is scanned, the stage can be moved using the z-control in order to scan another plane along the z direction. In this manner a three dimensional image of the specimen can be constructed. Pixel size is optimized using Nyquist criteria, pixel size = $\frac{resolution}{2.3}$. The resolution of the microscope in the X-Y plane and along the z direction are given by $d_{xy} = \frac{1.22\lambda}{2NA}$ and $d_z = \frac{2n\lambda}{NA^2}$, respectively, where n is the refractive index of immersion liquid used for the objective and λ is the wavelength of emitted light. It is clear that the z-resolution is poorer than the X-Y resolution for a given NA of the objective and wavelength of light.

Multiphoton excitation can also be used to excite the fluorophore instead of single photons. In that case confocality can be achieved without a pinhole, as the probability of excitation is proportional to the square of the incident intensity and emission from out of focal planes is extremely low. Using multiphoton excitation we can also avoid photobleaching of the entire sample although beaching occurs at the focal plane.

2.5 Preparation of giant unilamellar vesicles (GUVs)

There are several methods for the preparation of giant vesicles, reported in the literature [16, 17, 18, 19]. Vesicles in a aqueous solution can have heterogeneity in thickness (multilamellar with varying number of layers) and can be polydisperse in thier sizes. There are some necessary conditions associated with vesicle formation. For example, vesicles form only when the lipid is in the fluid (L_α) phase, which can be achieved by maintaining the temperature above the main transition of the lipid used. This is because the formation of vesicles involves bending of the membranes which is energetically expensive in the gel phase where the membranes are very rigid. High ionic strength of the solutions and high osmolarity can also prevent vesicle formation.

Electroformation method, first described by Angelova et al., is a popular and widely used protocol to prepare giant unilamellar vesicles [19, 20, 21]. Electroformation of vesicles produces mainly unilamellar vesicles of 10-100 μm diameter. Yield of unilamellar vesicles

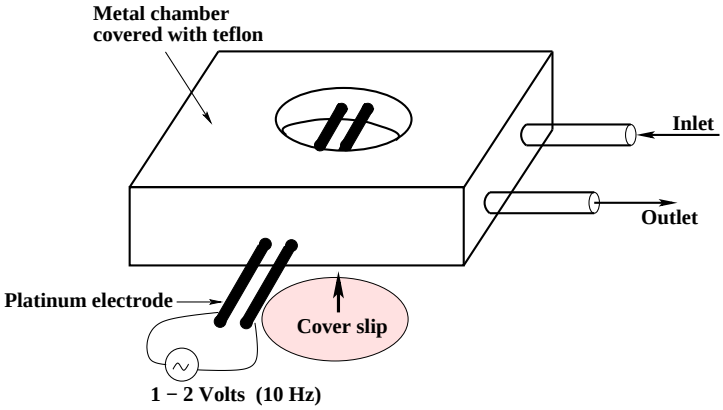

Figure 2.18: Schematic diagram of the chamber used for electroformation of GUVs.

Figure 2.19: A photographs of the chamber used for electroformation.

using eletroformation method is very high (95%) compared to other preparation methods [22]. We have designed a chamber for electroformation whose temperature is controlled by using a circulating water bath (*Julabo*). It consists of a hollow metal *Cu* block with an inlet and outlet for water circulation (Fig. 2.18). Two platinum wires were inserted through two-bore nonconducting ceramic tubes to avoid contact between the two electrodes. A circular coverslip is attached from the bottom using silicon glue, as shown in Fig. 2.18. The whole chamber is covered with a thin teflon sheet to increase its thermal stability. Fig. 2.19 is a photograph of the chamber used for electroformation of vesicles.

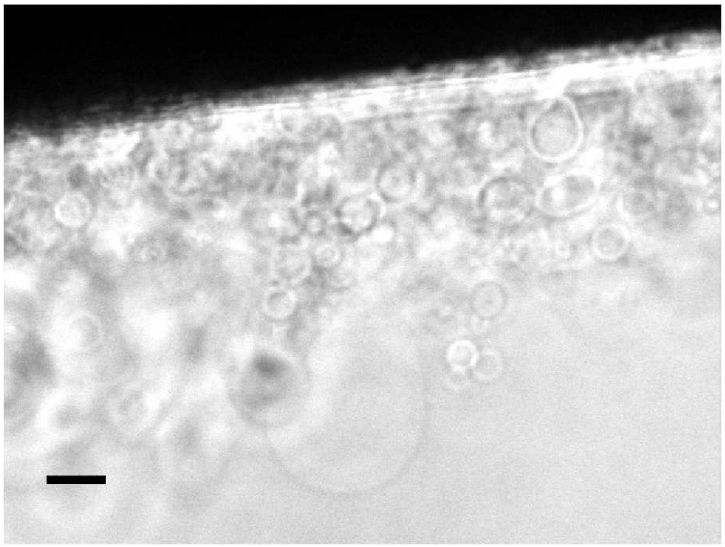

Figure 2.20: Electroformation of vesicles. Top black region is the image of part of the platinum electrode. Scale bar represents 10 μm.

2.5.1 Electroformation of vesicles

Stock solutions of the lipids and lipid–cholesterol mixtures of concentration 0.5 mg/ml were made in chloroform and were stored below 0°C. 1-2 μl of the stock solution was taken out using a Hamilton syringe and coated onto each platinum electrode and then the solvent was allowed to evaporate. For this technique to work the lipid film should not be too thick. The optimum thickness is in the range 10-100 bilayers. After removing all traces of the solvent, about 500 μl of Millipore water was added to the chamber and a 10-15 Hz alternating electric field (AC) of 1-3 volts amplitude was applied through the platinum electrodes. The temperature was maintained above the main transition of the lipid used. After about $1\frac{1}{2}$ hours the AC field was switched off. Vesicles form near the platinum wires, as shown in Fig. 2.20, and then they detach from the wires and form giant vesicles via coalescence (Fig. 2.21). Vesicles are poly-dispersed in size ranging from 10 - 100 μm.

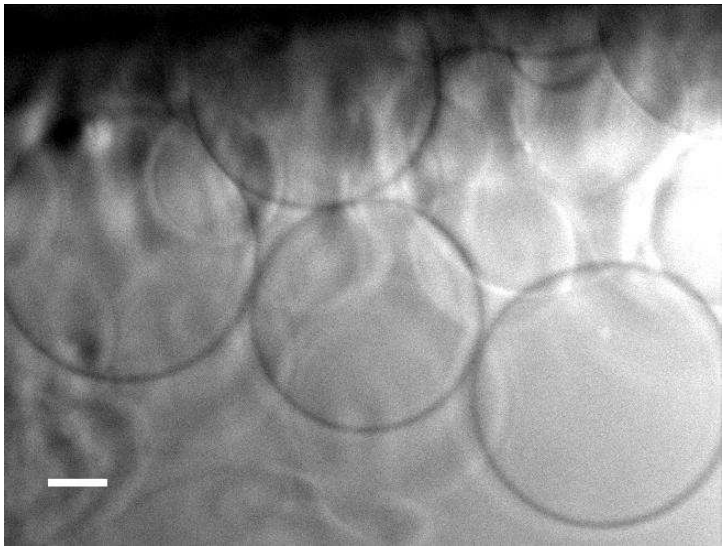

Figure 2.21: Phase contrast image of GUVs made from DOPC. Scale bar represents 10 μm.

Bibliography

[1] D. C. Champeney, *Fourier Transforms and Their Physical Applications* (Academic Press, London, 1973).

[2] G. H. Stout and L. H. Jensen, *X-ray Structure Determination* (The Macmillan Company, New York, 1968).

[3] A. Guinier, *X-ray Diffraction in Crystals, Imperfect Crystals, and Amorphous Bodies* (W. H. Freeman and Company, San Francisco and London, 1963).

[4] Y. K. Levine, Prog. Surf. Sci. **3**, 279 (1973).

[5] S. Tristram-Nagle, Y. Liu, J. Legleiter, and J. Nagle, Biophys. J. **83**, 3324 (2002).

[6] M. Hentschel and R. Hosemann, Mol. Cryst. Liq. Cryst. **94**, 291 (1983).

[7] Y. Lyatskaya, Y. Liu, S. Tristram-Nagle, J. Katsaras, and J. F. Nagle, Phys. Rev. E **63**, 011907 (2001).

[8] W. -J. Sun, S. Tristram-Nagle, R. M. Suter, and J. F. Nagle, Proc. Natl. Acad. Sci. U.S.A. **93**, 7008 (1996).

[9] D. L. Dorset, E. Beckmann, and F. Zemlin, Proc. Natl. Acad. Sci. U.S.A. **87**, 7570 (1990).

[10] J. Katsaras and M. J. Watson, Rev. Sci. Instrum. **71**, 1737 (2000).

[11] K. Sengupta, V. A. Raghunathan, and J. Katsaras, Phys. Rev. E **68**, 031710 (2003).

[12] T. J. McIntosh, Biochim. Biophys. Acta **513**, 43 (1978).

[13] W. H. Press, S. A. Teukolsky, W. T. Vetterling, and B. P. Flannery, *Numerical Recipes in FORTRAN* (Cambridge University Press, 1992).

[14] A. H. Bennett, H. Osterberg, H. Jupnik, and O. W. Richards, *Phase Microscopy Principles and Applications* (John Wiley and Sons, INC. London, 1951).

[15] J. R. Lakowicz, *Principles of Fluorescence Spectroscopy*, (Plenum Press, New York, 1983).

[16] F. M. Menger and K. D. Gabrielson, Angew. Chem. Int. Ed. Engl. **34**, 2091 (1995).

[17] A. Moscho, O. Orwar, D.T. Chiu, B. P. Modi, and R. N. Zare, Proc. Natl. Acad. Sci. U.S.A. **93**, 11443 (1996).

[18] K. Akashi, H. Miyata, H. Itoh, and K. Kinosita. Jr, Biophys. J. **71**, 3242 (1996).

[19] M. I. Angelova, S. Soléau, Ph. Méléard, J. E. Faucon, and P. Bothorel, Progr. Colloid. Polym. Sci. **89**, 127 (1992).

[20] M. I. Angelova and D. S. Dimitrov, Mol. Cryst. Liq. Cryst. **152**, 89 (1987).

[21] M. I. Angelova and D. S. Dimitrov, Faraday Discuss. Chem. Soc. **81**, 303 (1986).

[22] L. A. Bagatolli, T. Parasassi, and E. Gratton, Chem. Phys. Lipids **105**, 135 (2000).